Parameter Optimization for Accurate and Repeatable Strut Width in the 3D Printing of Composite Bone Scaffolds

Mahathir Mohammad Bappy [a], Emma Van Epps [b], Lauren B. Priddy [b], and Wenmeng Tian [a*]

[a] Department of Industrial and Systems Engineering, Mississippi State University, Mississippi State, MS 39762, United States

[b] Department of Agricultural and Biological Engineering, Mississippi State University, Mississippi State, MS 39762, United States

Abstract

Critically sized bone defects present a significant challenge to orthopedic surgeons due to the limited availability of autograft bone tissue, which is the current gold-standard treatment. As an alternative, 3D bioprinted porous scaffolds can be designed to mimic bone's mechanical and biochemical properties to support tissue regeneration. However, achieving high geometric accuracy and repeatability of these scaffolds can be challenging, especially when printing new composite materials and geometries. Therefore, the objective of this study was to optimize the extrusion-based 3D bioprinting process parameters for composite polymer-ceramic scaffolds. Bone scaffolds composed of a polylactic-co-glycolic acid (PLGA) and 5% nano-hydroxyapatite (nHA) composite were printed and analyzed to evaluate their dimensional accuracy, which is primarily determined by the process parameters. This empirical study investigated the effects of different process parameters, particularly, nozzle temperature, pressure, and printing speed, on the geometric accuracy (i.e., strut width) of the printed scaffolds. Starting with a full factorial design of experiments, *in-situ* layer-wise optical images were captured, which were then leveraged through image processing for strut width characterization. Subsequently, a new iterative process optimization method was proposed that involves regression modeling and bound constraint-based minimization. A case study on printing a two-layer scaffold was used to demonstrate the effectiveness of the proposed method. Overall, the geometric accuracy of the printed scaffolds improved significantly, maintaining a range of ±5% from the nominal strut width as iterative experiments were conducted, which demonstrates the significant potential of the proposed method in bioprinting process parameter optimization.

Keywords: 3D Bioprinting; Composite Material; Bone Scaffold; Process Parameter Optimization; Tissue Engineering.

1 Introduction

Bone tissue can self-heal only to a certain extent, and therefore bone grafts are often required for critically sized bone defects caused by trauma, tumor resection, osteoporosis, or congenital malformation [1,2]. Autografting is the gold standard for severe bone defects, but it is invasive and causes donor site morbidity [3]. Solid metal implants are an alternative treatment, but their higher Young's modulus than human bone can cause stress shielding-induced bone resorption that weakens and decreases bone density [4,5]. Moreover, grafts and metal implants are harder to customize due to the complex geometry of such defects. To alleviate the existing limitations, biodegradable composite scaffolds fabricated through 3D printing may serve as an effective alternative for bone tissue engineering [6]. The advantages of composite scaffold fabrication in bone tissue engineering include: a) geometric flexibility of 3D printing with controlled pore structure; b) customizable mechanical and biological properties by manipulating the material composition and geometry [7,8]. Specifically, composite scaffolds reportedly exhibit superior compressive strength and osteoconductivity compared to either polymer or ceramic alone [1,3,9].

Despite the unique flexibility and capabilities of composite scaffold 3D printing, the process involves significant challenges in quality control and process optimization. Basically, the intended pore structure and the necessary mechanical and biological properties can be obtained with carefully controlled geometric accuracy. The clinical effectiveness of a composite scaffold at facilitating bone in growth depends on geometric attributes like porosity and strut width, which must be highly customized and accurately characterized [10]. In order to achieve these long-term aims of tissue engineering, achieving the dimensional accuracy of 3D printed composite bone scaffolds is highly desirable [11,12]. However, the dimensional accuracy of 3D-printed scaffolds are determined by multiple factors, including raw material, binding agents, printing parameters, and post-processing treatments [13]. Scaffold geometric accuracy is enhanced by understanding the process variability and accordingly optimizing process parameters for the 3D printer [14]. Others have reported optimization of process parameters of various 3D printing or additive manufacturing (AM) processes (e.g., stereolithography [15], fused deposition modeling (FDM) [16], and selective laser sintering [17]). However, there are limited studies conducted to examine the impact of printing process parameters on the composite bone scaffold fabrication through extrusion-based printing. Therefore, this paper aims to establish a data-driven process parameter optimization method for customizable composite scaffold printing.

The objective of this study is to examine the geometric accuracy of the composite bone scaffolds through process parameter optimization. The composite material is comprised of a combination of biodegradable and biocompatible polylactic-co-glycolic acid (PLGA) and ceramic particles of nano-hydroxyapatite (nHA) that enhance stiffness and osteoconductivity [18,19]. The technical contributions of this paper are summarized as follows. First, an image analysis method is proposed to characterize the strut width obtained from scaffold printing based on the layer-wise *in-situ* optical images. Second, a new iterative regression-minimization model is established to find the optimum level of printing process parameters. Ultimately, this new scaffold printing process parameter optimization model can be applied to other scaffold printing systems with a different printer and/or material composition. This will enable the accelerated production of scaffolds with tailored properties, as well as reliable and repeatable geometric accuracy.

The remainder of the paper is organized as follows: A literature review on state-of-the-art composite scaffold printing and data-driven machine learning methods for 3D scaffold printing quality control is summarized in Section 2. The proposed methodology of material preparation, the initial design of experiment, image processing, and modeling and optimization framework are introduced in Section 3. In Section 4, the results are discussed. Finally, Section 5 presents the conclusion and future research directions.

2 Literature Review

This section briefly summarizes the state-of-the-art methodologies relevant to parameter optimization of 3D printed composite bone scaffolds. The major composite scaffold printing technologies are first summarized. Subsequently, the data-driven machine learning-based methods for optimization and quality control of 3D bioprinting are summarized. Lastly, the research gaps on process parameter optimization for composite scaffold printing are briefly discussed.

2.1 Composite Scaffold Printing

Various manufacturing processes, such as electrospinning and salt leaching, have been used to produce composite scaffolds that are both porous and biocompatible. However, these methods do not provide the specific customization for fabricating bone tissue implants for patient-specific bone defect geometries [20]. Although the microarchitectures produced by these techniques are well characterized, their geometries are limited to molds or manual processing [21]. This has motivated the exploration of a relatively modern method of scaffold fabrication: 3D printing. The primary motivation for using 3D printing techniques for scaffold fabrication is the control over strut or pore morphology, low cost, and relatively simple production process [20]. Of the many existing methods of 3D printing, FDM is highly compatible with thermoplastics, which can result in a stiffness value that is similar to human bone when mixed into a polymer-ceramic composite [19,20]. The unique ability to fine tune the polymer types and ratio of polymer to ceramic enables a wide range of stiffness values needed for fabricating a customizable bone tissue implant [7].

Current literature primarily reports the mixing of polymers (such as polylactic acid (PLA), polyglycolide (PGA), PLGA, and polycaprolactone (PCL)) with a bioceramic (such as hydroxyapatite (HA) or β-tricalcium phosphate (β-TCP)) to obtain an appropriate composite material for use in 3D printing [3,22–24]. The degradation rate, acidic byproducts, and mechanical properties of the above polymers must be considered when selecting an appropriate polymer for composite preparation. Additionally, the addition of a bioceramic can alter the composite's viscosity during processing [25,26]. HA, the crystalline form of calcium phosphate, is commonly used in orthopedic implant research due to its chemical similarity to the mineral component of human bone tissue [1,5,27]. The mineral is both bioactive and can improve a scaffold's osteoconductive properties due to its hydrophilicity and capacity to increase polymer surface roughness. When bound to a polymer, it creates a more favorable surface topography for cell adhesion [22]. Nanohydroxyapatite (nHA) is especially effective because its increased surface area creates an ideal nanotopography for promoting cell adhesion [28]. The percentage of ceramic dispersed in the polymer is also an area of interest. Literature reports a wide variety of HA concentrations ranging from 0%, 5%, and up to 50% HA in polymer scaffolds [22], [29,30]. Thus, optimizing the printing parameters for such a wide range of concentrations has become a highly empirical process. Variations in the choice of polymer and brand of 3D printer have also contributed to the inconsistencies in printing. Therefore, there is an urgent need to establish an efficient process for parameter optimization for composite scaffold printing.

2.2 Experimental Parameter Optimization for 3D Bioprinting Applications

In the rapidly evolving field of bioprinting, the investigation of optimal printing parameters is very significant to achieving precise, reproducible, and biocompatible constructs. Numerous experimental studies [31–34] are continuously explored, with the most relevant ones being discussed within this section. For instance, an experimental parameter optimization method is developed for 3D printing of hydrogels by evaluating multiple printing parameters in a standardized manner applicable to extrusion-based bioinks [35]. Similarly, optimization of starch and chitosan-based bio-inks in 3D bioprinting of scaffolds for neural cell growth was also performed [36], where the printability and biocompatibility of different starch-to-chitosan ratio bioinks were examined. In addition, an experimental study was conducted to use 3D printing in the fabrication of SA-GEL (sodium alginate and gelatin) porous cartilage scaffolds with optimal parameters [37]. Moreover, experimental analysis based on design of experiments (DOE) has been applied for process parameter optimization, leading to significantly improved geometric accuracy and compressive modulus of thermoplastic- and hydrogel-based tissue scaffolds [38]. Furthermore, it is reported that the fiber spreading ratio on simple serpentines and volumetric dispensing system play vital roles in determining optimal printing parameters in Martigel scaffolds printing [39]. A study on parameter optimization of 3D bioprinting using hybrid bioinks was performed, and it was demonstrated that the printing quality is affected by the combination of a large variety of parameters [40]. Moreover, research has explored the optimization and fabrication of customized scaffolds to match human bone properties, utilizing a numerical study validated by experimental routines. This approach enables the optimization, fabrication, and automation of generating open porous polyamide scaffolds [41]. Based on a study of the literature, it is prominent that the pursuit of optimal printing parameters extends across various domains of bioprinting, each presenting unique challenges and considerations.

2.3 Data-driven Machine Learning (ML)-Based Process Parameter Optimization of Composite Scaffold 3D Printing

Data-driven ML-based methods have gained considerable attention in recent years for optimizing process parameters in the 3D printing of bone scaffolds [42]. By leveraging data-driven approaches, the optimal combination of process parameters can be identified which can enhance the mechanical properties, biocompatibility, and overall quality of the 3D printed scaffolds [43–45]. Several studies have explored the use of data-driven algorithms, such as artificial neural networks (ANN), genetic algorithms, and response surface methodology, to analyze large datasets and uncover complex relationships between process parameters and scaffold properties. For instance, a multi-objective genetic algorithm is developed for printing parameter optimization of polycaprolactone/hydroxyapatite composite scaffolds, achieving improved mechanical strength and porosity [46]. Similarly, an ANN-based model was leveraged for printing parameter optimization of poly (lactic-co-glycolic acid)/β-tricalcium phosphate scaffolds. The ANN model successfully predicted the optimal parameter combinations, resulting in enhanced scaffold mechanical properties [47,48]. In addition, response surface methodology has been utilized to optimize the process parameters of a silk fibroin/calcium phosphate composite scaffold, achieving improved compressive strength and pore size distribution [49,50]. Furthermore, the deep neural network-based algorithm was applied in parameter optimization of multiple quality outputs. This method also allows user selection within the optimal process parameters for fabricated products with conforming product properties [51]. Moreover, 3D printing and ML has been recently integrated to facilitate the selection of optimal printing parameters, which can reduce the number of error-and-trial experiments needed for printing parameter optimization [52]. Although data-driven ML-based methods have shown significant potential for optimizing process parameters for scaffold 3D printing, further research is needed for the development of highly customized and functional composite bone scaffolds for tissue engineering applications.

2.4 Data-driven Methods for Quality Control of Bioprinting

Online sensors can provide data for the real-time quality control of the 3D printed scaffolds during fabrication. It can specifically monitor the printing fidelity and geometric morphology of the printed parts using an integrated machine vision system [53]. The sensing-based approaches can be categorized into two distinct groups: (i) real-time monitoring for anomaly detection only and (ii) real-time monitoring and process control. For instance, a recent study investigated the use of ML for anomaly detection in distinguishing between printing configurations that are likely to result in low-quality prints and printing configurations that are more promising as a first step towards the development of a recommendation system [54]. Similarly, a convolutional neural network (CNN) model is designed to achieve efficient defect classification of the FDM parts considering the surface data with high accuracy [55]. In addition, in many manufacturing applications, CNN-based classifiers are used for defect detection and can be employed in process monitoring and correction in 3D printing, where visual features can be learned to extract critical information from the raw images. This approach would enable the fabrication of 3D-printed structures with high accuracy and repeatability [56].

On the other hand, for real time monitoring and process control, sensors like temperature, CO2, and humidity are needed to monitor and accordingly adjust the printing environment by integrating a closed-loop feedback mechanism and a computer vision-based control system [57,58]. Moreover, using optical coherence tomography (OCT), the 3D microstructure of melt electrowriting scaffolds was recently reported. The microstructural characteristics can be calculated from OCT data using a custom method that shows excellent agreement with scanning electron microscopy (SEM) results [59]. Another example is the development of a real-time monitoring and autonomous correction system, where a deep learning model and a feedback loop are integrated to adjust 3D-printing parameters of FDM in an iterative and adaptive manner [60].

2.5 Research Gaps and Technical Contributions

This section discusses the research gaps based on state-of-the-art experimental and data-driven methodologies relevant to process parameter optimization of 3D-printed composite bone scaffolds. The existing process parameter optimization techniques have made progress. However, there are still some limitations, which include limited exploration of (i) parameter interactions, (ii) novel composite material behavior based on process parameters in extrusion-based 3D printing, (iii) the time-consuming nature of iterative experimentation for parameter optimization, and (iv) difficulty in achieving consistent reproducibility across different bioprinting platforms and materials with a process-specific optimized parameter. Besides these, for ML-based methods, a larger dataset enables the development of robust ML algorithms. While most methods guide the determination of optimum printing parameters, real-time monitoring of the 3D printing process can enable live adjustment of printing parameters upon detection of any deficiencies during the printing process. Addressing these limitations will significantly advance the field of process optimization for 3D composite scaffold printing, leading to enhanced geometric accuracy of scaffold and more efficient production processes. Specifically, despite the growing body of literature on the optimization of process parameters in 3D scaffold printing, there is a notable research gap in the exploration of the interaction effects of temperature, pressure, and speed in the context of novel composite material extrusion processes. Existing studies have largely focused on individual parameter optimization, overlooking the potential synergistic effects and their impact on scaffold geometric accuracy and fabrication repeatability.

The technical contribution of this paper is summarized below. By applying regression minimization modeling, the proposed method explains the intricate relationships between various printing parameters and resulting strut width, offering insights into their impact on the 3D printing of composite scaffolds. Along with the enhancement of understanding of complex interactions, this study generates the optimal process parameters for achieving the desired strut width. Essentially, by leveraging empirical data and ML modeling, this study develops a structured approach for identifying optimal process parameters, enhancing reproducibility, and reducing the dependence on extensive trial-and-error experiments.

3 Proposed Methodology

This section is comprised of the materials and methods employed for the optimization of the composite material printing process, utilizing a combination of Design of Experiments (DOE), image analysis for strut width characterization, and a modeling and optimization framework. Basically, the DOE approach is utilized to systematically vary the process parameters and evaluate their effects on scaffold properties. Additionally, image analysis techniques were employed to characterize the strut width of the printed scaffolds, providing quantitative measurements for further analysis. Finally, a modeling and optimization framework was developed to establish predictive models and optimize the process parameters for scaffold printing. This comprehensive approach combining composite material printing process optimization, DOE, image analysis, and modeling provides a structured methodology for enhancing the geometric accuracy and functionality of 3D printed composite bone scaffolds.

3.1 Composite Material Preparation and Scaffold Printing

The composite material for scaffold fabrication was prepared in a stepwise manner to ensure proper mixing, elimination of solvents, and loading into the printing cartridge for subsequent 3D printing. First, pellets of PLGA (CELLINK, Blacksburg, VA, USA) with a PLA-PGA ratio of 50:50 and an inherent viscosity of 0.65 dL/g, and hydroxyapatite nanospheres (nHA) (Sigma-Aldrich., St. Louis, MO, USA) with a molecular weight of 502.31 g/mol, a diameter <200 nm, and ≥97% apatite purity were used to prepare the composite material. The composite material was prepared as 5% nHA and 95% PLGA by weight. Acetone was used as the solvent for mixing, and the ratio of acetone to PLGA-nHA composite was 3:1 (vol:mass).

The material was prepared in 2 g batches in a 200 mL beaker to maximize the exposed surface area and promote acetone evaporation. The solution was covered and stirred at 70 rpm for 2 hours at room temperature. The material was then uncovered, and the solution was mixed uncovered at the same speed overnight at room temperature. The composite material was then incubated at 75°C for 12-15 hours to ensure solvent evaporation. The initial dry weight of PLGA and nHA was compared to the final composite material weight after acetone evaporation to ensure thorough elimination of solvent (<100mg solvent remaining). The composite material was stored in a desiccator until use for up to two weeks. Finally, to load the finished material into the printing cartridge, the composite was heated to 150°C for 5 minutes on a heating plate. Once softened, the composite was scooped into the printing cartridge and pressed to the bottom with a plunger. The handle of the plunger was then removed, and the plunger end remained in the cartridge to ensure even force was applied to the material by the pressurized air. The material preparation process is outlined in Figure 1.

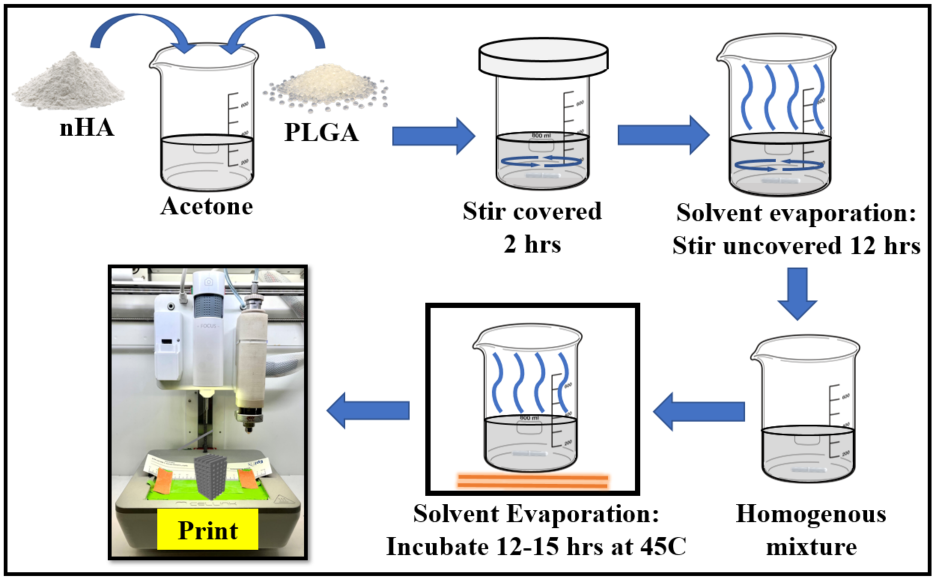

Figure 1: Composite material preparation process

The 3D model of the scaffold was designed using Tinkercad software with a strut width of 0.4 mm, a layer height of 0.4 mm, and a pore size of 750 µm (Figure 2). Here, the pore size of 750 µm refers to the dimensions of the unprinted hollow square regions between the struts. These parameters were selected to achieve the desired structural design and pore size in the final printed scaffold.

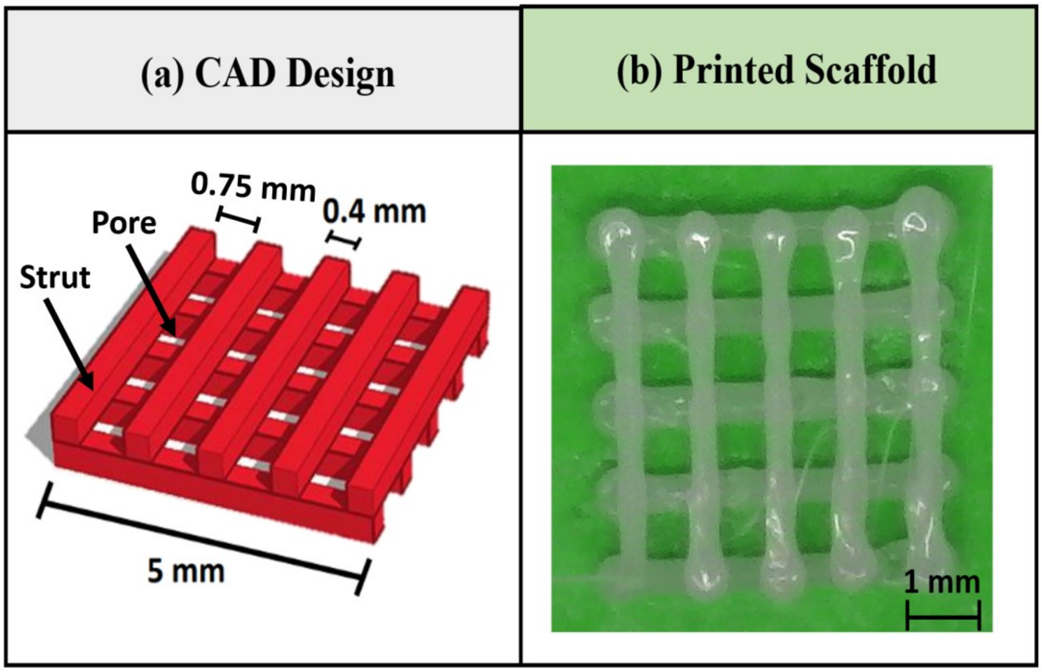

Figure 2: (a) CAD design and (b) a printed scaffold

The process of material extrusion consists of a pressure pump that delivers filtered air into the material cartridge and a heating element located just above a 0.4 mm diameter nozzle. This pressurized system forces the heated material through the nozzle to create a uniform, viscous flow. This printing setup provides control over the temperature, pressure, and printing speed of the material. The infill rate was set to 100%, and a rectilinear infill pattern was selected for printing. In 3D printing, the infill ratio is an important parameter that represents the fill rate of the part to be produced. It refers to the density of material used to fill the interior of the design object. In the study, an infill ratio of 100%, suggests that the interior of the printed object is completely filled with material, while the pore size of 750 μm is associated with the design of the scaffolds. More specifically, it refers to the spacing between the struts of the scaffold, as demonstrated in Figure 2(a). Moreover, in Figure 2(a), to enhance clarity, the label information for both the strut and pore is also included, along with their respective dimensions. In this study, scaffolds were printed using the CELLINK BIO X printer's thermoplastic printhead. An advantage of the BIO X is its ability to capture layer-wise images of the scaffold during printing. Top-down images were taken after each layer for subsequent analyses. Furthermore, double sided tape was used to facilitate the image analysis process by providing high contrast between the struts and the background. We used a brightly colored tape on top of the baseplate of the printer to provide higher image contrast. Furthermore, we expect the tape had little to no effect on the second layer of the scaffolds, which was the layer that was analyzed. In the scenario of fabrication for real-world medical use, a heated baseplate would be used rather than the tape. However, only for the purpose of printing parameter optimization, we utilized the double-sided tape as a substitute. The printing setup is demonstrated in Figure 3.

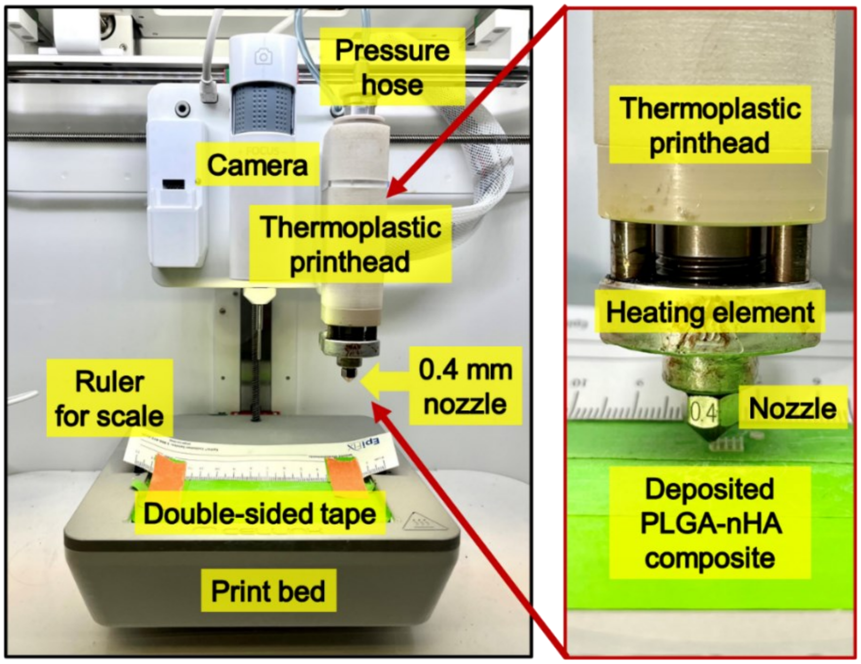

Figure 3: The setup for composite bone scaffold printing.

3.2 Proposed Framework

Figure 4 represents the proposed iterative method for optimizing the process parameters in 3D scaffold printing. The objective is to enhance the quality and performance of the printed scaffolds by systematically refining the parameters that govern the printing process. The method incorporates initial experimental designs, image analysis for strut width characterization, and a modeling and optimization framework. Initially, a set of process parameters is selected, and scaffold samples are printed with layer-wise images collected and strut width characterized. Image analysis techniques are employed to characterize the strut width of the printed scaffolds, providing quantitative data for analysis. Subsequently, a mathematical model is developed to describe the relationship between the process parameters and the strut width. The model is calibrated and validated using the data obtained from the initial experiments. Optimization algorithms are then applied to explore the parameter space and identify the optimal combination of process parameters that optimizes the strut width. The process iterates, updating the model with new data, refining the process parameters, and repeating the printing and analysis steps until the optimization criteria are met.

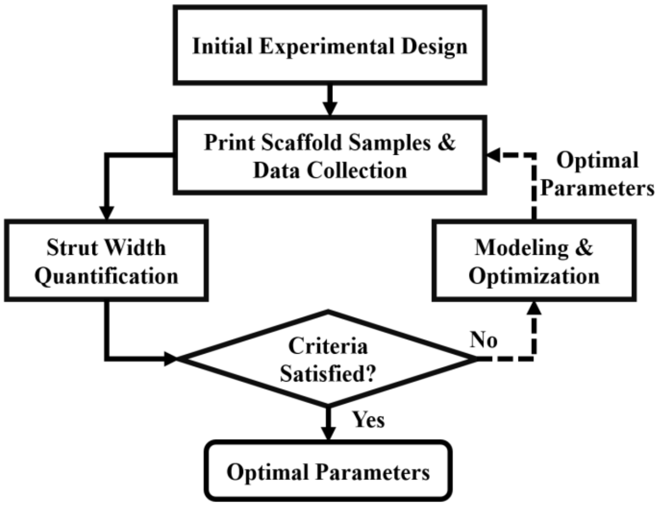

Figure 4: Flowchart of the proposed iterative method for process parameter optimization in composite scaffold printing.

3.2.1 Initial Experimental Designs

A full factorial experimental design is used as the initial experimental design for printing the composite scaffolds. The factorial design helps to study the effects caused by independent factors and interactions between those self-governing factors [61,62]. In this work, three independent factors (i.e., temperature (X_t), pressure (X_p), and speed (X_{sp})) are used. In addition, three factorial levels are leveraged for the experimentation in this study. The levels of these parameters are selected with the help of a machine manual and by performing the preliminary test on a 3D bioprinter. On the basis of preliminary experimentation, the ranges and, subsequently, the levels of the printing parameters are chosen as shown in Table 1. Moreover, based on a random full factorial DOE, a total of 27 experimental runs are generated for analyzing the interaction of each level on scaffold printing, and in this study, strut width is considered a response factor.

Table 1: Independent factor levels of initial experiments

Independent factors	**Levels**		
Temperature (°C)	115	120	125
Pressure (kPa)	225	250	275
Speed (mm/s)	1	1.5	2

3.2.2 Image Analysis for Strut Width Characterization

An image processing approach is developed to measure the strut width from the layer-wise captured scaffold images during printing. The key concept was to distinguish the pixels of the strut region from other regions in the image and to derive the strut width based on the pixel data. Essentially, for image processing, four key steps are followed, as depicted in Figure 3. The key steps for image processing are as follows:

Step 1: Extracting regions of interest (ROI) from RGB images: For each experiment, layer-wise images were acquired through an optical camera. Each image is not analyzed for all regions at once but divided into appropriate ROIs for analysis Regarding the selection of rows in the scaffolds, only the most recent layer was considered as the appropriate region for further analysis. Moreover, each scaffold was examined at specific locations or rows within the scaffolds, making sure that these regions were selected to be indicative of the scaffold's overall strut. Specifically, in Equation (1), each cropped region is considered to be a combination of the number of rows of pixels that are averaged and combined to get the strut width. It is noted that the brightness distributions of the strut and surrounding base can be different. Therefore, to obtain more accurate results, analysis was performed by dividing the image into several segments.

Step 2: Image pre-processing by converting an RGB image into a grayscale image: As the original image of a segment was a combination of red, green, and blue colors, it contained a significant amount of data. Therefore, this image was simplified to a grayscale image with only brightness information, which changes the intensity values from 0 to 255.

Step 3: Image binarization: After image simplification, an appropriate threshold was determined to filter out the pixels in the strut region. This threshold was determined by analyzing the histogram information of the image brightness. For generating binary images, the brightness of each pixel was compared to the threshold value, and it was converted to white or black depending on the brightness. Through this process, the grayscale image was converted into a binary image expressing strut regions and other regions.

Step 4: Strut width quantification and pixel size unit conversion: The number of pixels in the strut region is leveraged for the quantification of strut width. The size of the pixels in the real-time images depends on the magnification during imaging. Therefore, it is necessary to convert the pixel to a metric unit (i.e., mm) in order to obtain the final measurements on a unified scale, independently from the scale factor of imaging. Basically, during the image capturing process, we ensured the presence of a millimeter scale within the field of view. This millimeter (mm) scale serves as a reference for establishing the conversion from pixels numbers to length in mm scale. Then, we counted the number of pixels corresponding to the known length on the mm scale within the image. After that, by dividing the number of pixels by the known length in millimeters, we derived the pixel-to-length ratio. Finally, the reciprocal of the pixel-to-length ratio gives us the unit conversion factor, denoted as u = 1 / (Number of pixels per millimeter). It's important to note that this width measurement is not based on a single row of pixels, but rather on data aggregated from all the rows in the ROI collectively. Each ROI provides a data point contributing to the average width measurement, thereby incorporating information from various sections of the scaffold. For clarity, the formulation of the width calculation is represented using equation (1) as follows:

$$Y = \left(\frac{\sum_{i=1}^{r} \sum N_{bright}(i)}{r}\right) \times u \tag{1}$$

where Y denotes the strut width and $(i = 1,2, \ldots r)$ denotes the number of rows in the region of interest of a strut for width computation. N_{bright} denotes the bright pixel in the region of interests as shown in Figure 5 and u denotes the unit conversion factor.

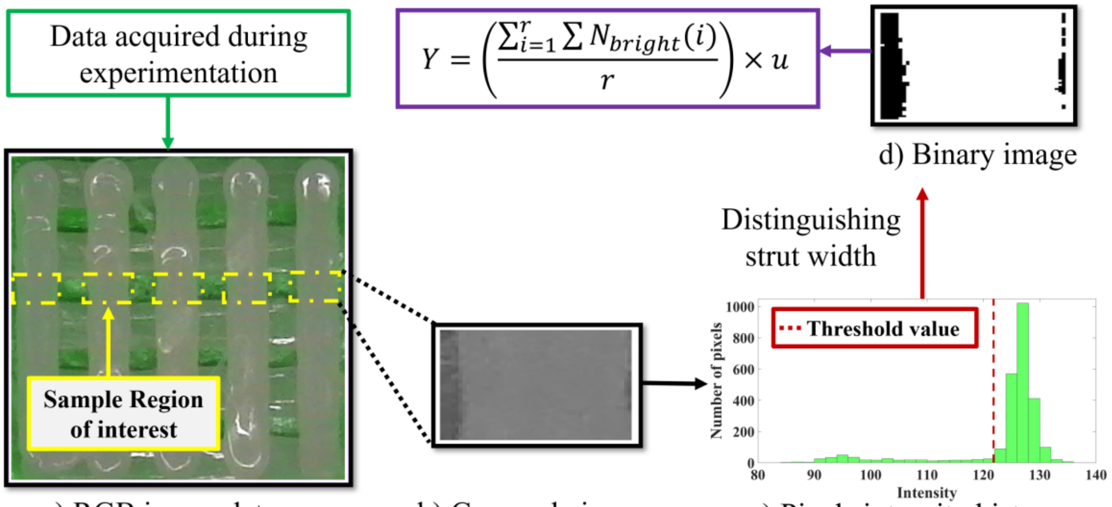

a) RGB image data b) Grayscale image c) Pixels intensity histogram

Figure 5: Image processing flow chart for strut width quantification

3.2.3 Modeling and Optimization Framework

In this section, a comprehensive modeling and optimization framework is presented specifically tailored for optimizing strut width (Y), focusing on the scenario where three independent factors of temperature (X_t), pressure (X_p), and speed (X_s) influence Y. Basically, after experimentation and image processing, for capturing nonlinear effects and interactions between variables, polynomial regression can be well suited for this problem [63]. Therefore, a quadratic polynomial regression model was assumed for predicting individual Y variables. The regression model describing the functional relationships between independent variables (X_t, X_p, X_s) and a single dependent variable Y, can be generalized as follows:

$$\begin{aligned} Y = \beta_0 + \beta_t X_t + \beta_p X_p + \beta_s X_s + \ldots & \quad \text{Intercept \& first order terms} \\ \beta_{tt} X_t^2 + \beta_{pp} X_p^2 + \beta_{ss} X_s^2 + \ldots & \quad \text{Quadratic terms} \\ \beta_{tp} X_t X_p + \beta_{ts} X_t X_s + \beta_{ps} X_p X_s + \ldots & \quad \text{Interactions terms} \\ \varepsilon & \quad \text{Error term} \end{aligned} \tag{2}$$

where β_0, $(\beta_t, \beta_p, \beta_s)$, $(\beta_{tt}, \beta_{pp}, \beta_{ss})$, $(\beta_{tp}, \beta_{ts}, \beta_{ps})$ are intercept, linear, quadratic, and interaction regression coefficients, respectively. The error term is represented by ε, and based on the central limit theorem, it is usually assumed that the error term follows a Gaussian distribution with a mean of 0 and a standard deviation of σ_ε. Specifically, ten regression coefficients need to be estimated, as observed from equation 2. During analysis, among different statistical attributes, the adjusted R squared value can be quantified as a criterion of the fit between the data and the regression [63,64]. The predicted response values and the estimated regression coefficients can be obtained using quadratic polynomial regression with arbitrary input values. Usually, there should be a minimum difference between the nominal strut width and the predicted response. Therefore, to obtain the optimized process parameters, a loss function $\mathcal{L}(X_t, X_p, X_s)$ can be developed with the fitted model along with estimated coefficients and nominal strut width (N_t) as follows:

$$\mathcal{L}(X_t, X_p, X_s) = \begin{pmatrix} \hat{\beta}_0 + \hat{\beta}_t X_t + \hat{\beta}_p X_p + \hat{\beta}_s X_s + \hat{\beta}_{tt} X_t^2 + \hat{\beta}_{pp} X_p^2 + \hat{\beta}_{ss} X_s^2 + \hat{\beta}_{tp} X_t X_p + \\ \hat{\beta}_{ts} X_t X_s + \hat{\beta}_{ps} X_p X_s - N_t \end{pmatrix}^2 \tag{3}$$

Furthermore, to obtain the optimized values of the independent variables for achieving nominal strut width, the minimization problem can be formulated with bounded constraints as follows:

$$\text{minimize:} \quad \mathcal{L}(X_t, X_p, X_s) \tag{4}$$

$$\text{subject to:}\quad \begin{aligned} l_t &\le X_t \le u_t \\ l_p &\le X_p \le u_p \\ l_s &\le X_s \le l_s \end{aligned}$$

where $\mathcal{L}(X_t, X_p, X_s)$ is the objective function that needs to be minimized, and $l_t \le X_t \le u_t$ denotes the lower (l_t) and upper (u_t) bounds for variable X_t respectively. The goal is to find the values of $X_t, X_p,$ and X_s that minimize the function $\mathcal{L}(X_t, X_p, X_s)$, subject to the given constraints on the variables. The constraints on the variables are given by the inequalities to ensure that the values of the variables will be within the specified bounds during the optimization process. Bounded constraints are important because they define a feasible region within which the optimization algorithm can search for the optimal solution. By limiting the solution space to a specific range of values, bounded constraints help ensure that the optimization process remains practical and relevant to the real-world problem being solved. As the optimization problem is bounded constraints, therefore, the adopted technique to solve the problem should support the bounded constraints. Considering the specific problem and the properties of the objective function and constraints, the L-BFGS-B algorithm [65] is adopted, which is a limited-memory algorithm for solving large nonlinear optimization problems subject to simple bounds on the variables. Thus, by formulating and solving the minimization problem, a set of optimized parameters for independent variables can be obtained as: $\{X_t^*, X_p^*, X_s^*\}$.

To evaluate the regression-minimization model's performance, with the optimized parameters, the printed strut width can be compared with the nominal strut width for observing deviations. Essentially, it is important to define the acceptable or satisfactory range around the target nominal strut width, providing a quantitative criterion for assessing the performance of the printed scaffolds. In this study, we aim to minimize the average printing error by optimizing the process parameters for scaffold printing. However, natural process variations can always occur during printing, making it impossible to achieve the exact nominal values consistently. Therefore, we incorporated upper and lower limits to account for these variations and make them the stopping criteria of our proposed optimization framework. In this study, ±5% tolerance ensures that slight variations in the strut width are considered within a satisfactory or acceptable range [Upper Limit: Nominal Strut Width + (Nominal Strut Width × 0.05); Lower Limit: Nominal Strut Width - (Nominal Strut Width × 0.05)] while maintaining the desired design specifications. Thus, if the model's performance is not satisfactory, it can be updated to improve its performance, as depicted in Figure 4. The model update involves modifying the model structure by incorporating the iteratively generated sample data for evaluation. Specifically, the new measurements are incorporated into the modeling, and the regression model is updated using the combined dataset, including both the initial training data and the newly measured dimensions. This will iteratively adjust the model to improve its accuracy. Basically, the iteration is performed by printing additional samples with updated parameter combinations, measuring the strut width, and updating the dataset and regression-minimization model. The number of iterations depends on the desired level of accuracy and the convergence of the model. Once the model has converged to the desired accuracy level, it can be used to predict the nominal dimension for any given set of printing parameters. This prediction provides an estimate of the expected dimension based on the learned relationship from the training data. Thus, this approach can iteratively refine the model to improve its accuracy in predicting the geometric dimension in 3D bioprinting of composite bone scaffolds and also consider the variability and dependencies of the printing process parameters on the resulting dimensions. The proposed iterative process optimization flowchart is summarized in Figure 6.

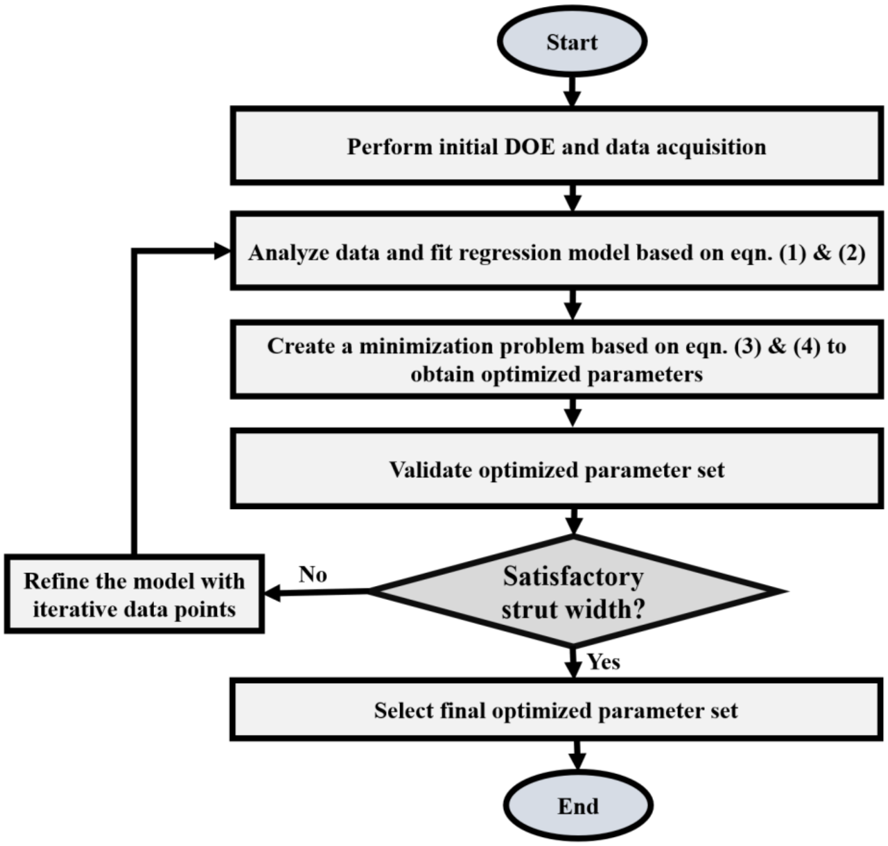

Figure 6: Flowchart of the proposed iterative process parameter optimization method.

4 Results and Discussion

In this section, the experimental data are used to evaluate the process parameter optimization model. For predictive modeling, a set of 135 regions of interest (ROI) samples is generated from 27 printed scaffolds based on a full factorial DOE. Specifically, each scaffold is measured at 5 locations, and our methodology was designed to ensure that these locations were chosen to be representative of the overall structure of the scaffolds. Specifically, each ROI includes a collection of rows of pixels, which are averaged to obtain the average strut width in the ROI. Moreover, our iterative improvement of the initial model by printing more scaffolds highlights one of the strengths of our study: the ability to handle and derive meaningful insights from relatively small experimental datasets. It is worth noting that, prior to the experiment, the delay between image capture and the print resuming often caused small blockages in the nozzle, presumably due to material cooling, resulting in layers with abnormally short first struts. Thus, a separate small cylinder was printed alongside each scaffold, allowing any blockages to be extruded prior to printing each new layer of the scaffold. Essentially, the generated samples are characterized by image processing for strut width quantification, as described in Section 3.3. The resulting strut width over the samples for 27 experimental arrangements is depicted in Figure 7. To construct each boxplot and interaction plot in the figure, 45 data points were utilized, enabling a comprehensive analysis of both dependent and independent variables. In this case, the nominal strut width is 0.4 mm, which needs to be obtained with optimized process parameters. The nominal strut width is defined as 0.4 mm as an arbitrary scaffold design. However, it's important to note that this value does not restrict the generality of the model. Rather, it can serve as a baseline for the iterative optimization process. In essence, the modeling approach described in the study remains applicable regardless of the specific nominal strut thickness chosen.

The resulting boxplot visualizes the relationship between the independent variables (i.e., temperature, pressure, and speed) and the width of struts. For example, it is observed that there is a positive correlation between the two variables (i.e., as the temperature and pressure increase, the strut width also tends to increase), whereas a negative correlation is observed for the variable of speed because when speed increases, the strut width decreases. Moreover, in Figure 7 the interaction plots describe the effect of one independent variable on the strut width changes for different levels of the other independent variable and how this relates to the overall interaction pattern. Specifically, from Figure 7, some assumptions about the combined impact of the process parameters can be made for setting the printing process parameters. It is observed that when the temperature and pressure are closer to the lower bound as well as the speed is closer to the upper bound, there is a potential to obtain the nominal print width.

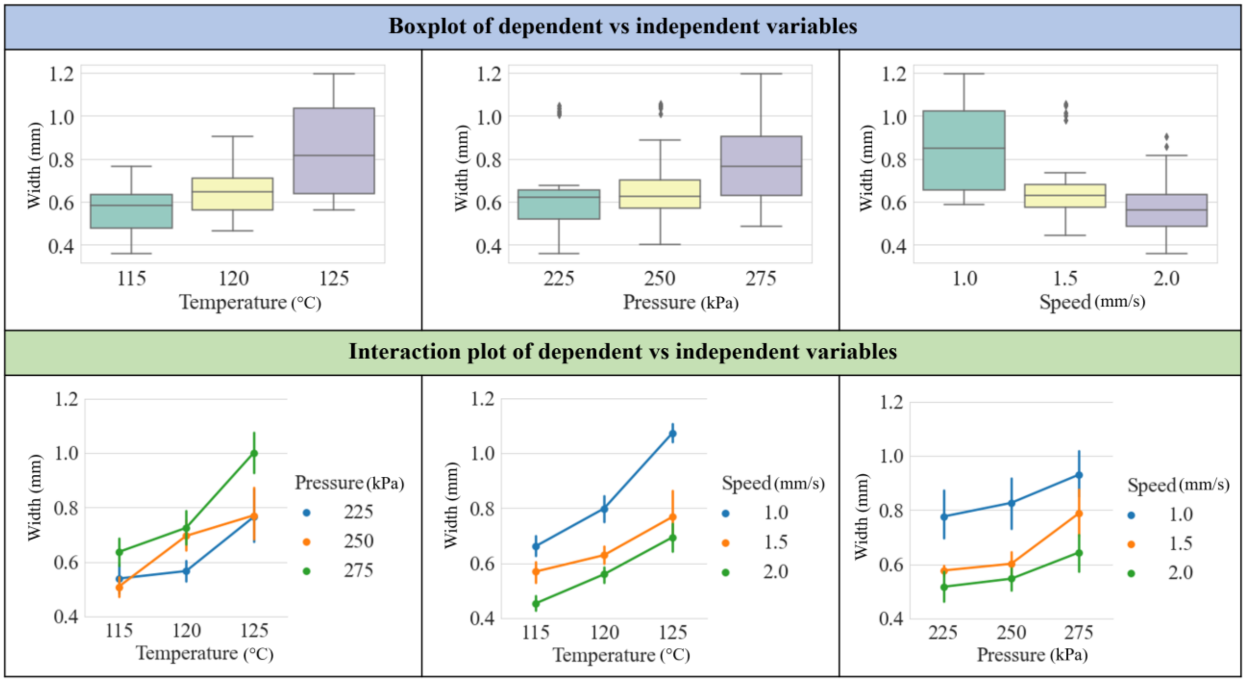

Figure 7: Plotting of strut width with different sets of independent process parameters.

Based on the experimentation, for robust process parameter optimization, after characterizing the strut width, the regression model is leveraged, considering the input and response variables. Based on the modeling, regression coefficients, obtained by employing a least squares technique to predict a quadratic polynomial model for the response variable, are summarized in Table 2.

Table 2: Regression results of predicted quadratic polynomial model.

Variables	Coefficients	Std. err.	p-value
Intercept	31.0986	7.897	0.000
X_t	-0.4136	0.125	0.001
X_p	-0.0688	0.014	0.000
X_s	1.2307	0.511	0.018
X_t^2	0.0016	0.001	0.002
$X_t X_p$	0.0003	7.34e-05	0.000
$X_t X_s$	-0.0167	0.004	0.000
X_p^2	6.868e-05	2.13e-05	0.002
$X_p X_s$	-0.0006	0.001	0.432
X_s^2	0.2114	0.052	0.000
R-square	**0.897**	**F-statistic**	**95.17**
Adj. R-squared	**0.888**	**DF model**	**9**

For the strut width prediction, the evaluation of these coefficients with the p-value indicated that linear and quadratic terms of the independent variables are highly significant. From Table 2, it is observed that most of the variables demonstrate almost zero p-values. In statistical hypothesis testing, a smaller p-value suggests stronger evidence against the null hypothesis, indicating that the observed results are unlikely to have occurred by chance [66,67]. Furthermore, a p-value less than a predetermined significance level (typically 0.05) indicates that we have sufficient evidence to reject the null hypothesis, suggesting that the corresponding term in the model is statistically significant. Therefore, having p-values close to zero signifies the significance of the variables included in the model [67–69]. In this case, there is no significant interaction between pressure and speed for the response variables. Therefore, generally, these results suggest that all linear, quadratic, and interaction effects (without interaction between pressure and speed) of the independent factors could potentially be the primary determining factors affecting the response variables. These results also denote that the regression models predicted for Y are significant with satisfactory coefficients of determination (R2) and (adj. R2), 0.897 and 0.888, respectively. Based on the determined coefficients, the objective function described in Section 3.4 can be formulated as follows.

Minimize:

$$(31.09 - 0.4136X_t - 0.0688X_p + 1.2307X_s + 0.0016X_t^2 + 0.000068X_p^2 + 0.2114X_s^2 + 0.0003X_tX_p - 0.0167X_tX_s - 0.4)^2$$

$$\text{subject to:} \quad 115 \le X_t \le 125$$

$$225 \le X_p \le 275$$

$$1 \le X_s \le 2$$

The minimization objective function with the bound constraints is leveraged as mentioned in the approach in Section 3.4. The L-BFGS-B algorithm [38] is adopted for solving the minimization problem, and thus a set of optimized parameters for temperature, pressure, and speed can be obtained as follows: $\{X_t^*, X_p^*, X_s^*\}$ following the proposed methodology. Based on the optimization results, the parameters are used for the corresponding experimental validation. This approach aligns with previous research demonstrating the importance of parameter optimization in achieving desirable outcomes in 3D printing applications. For example, previous studies have underscored the importance of optimizing strut width to enhance the mechanical properties and structural integrity of 3D-printed scaffolds [70,71]. Similarly, the critical role of strut width in controlling porosity and pore size distribution within printed scaffolds is also emphasized, which directly impacts the biological performance of scaffolds [72]. Moreover, researchers have recognized the critical importance of precise control over strut width to attain uniformity and reproducibility in scaffold fabrication [73]. Despite differences in materials and designs, the studies mentioned are closely aligned with the objectives of this research, which aims to achieve consistent and precise scaffold printing with particular emphasis on controlling strut width. In this study, with the optimized parameter, the printed scaffold along with the quantified width of multiple samples can be depicted, as demonstrated in Figure 8. The boxplot with error bars (red color) in Figure 8 displays the distribution of the width of the printed scaffold samples across different iterations. It provides a visual summary of key statistics, such as the mean (blue color line) and quartiles of the distribution for three different iterations. Basically, the error bars indicate the uncertainty associated with the data points. It is observed that, for iteration 2 with $\{X_t^*, X_p^*, X_s^*\} = \{115, 249, 2\}$, the mean line is close to the nominal width, and the error bars are also within the acceptable range. Ultimately, it is assumed that it is feasible and reasonable to guide the composite bone printing process with 3D bioprinting by using optimized process parameters.

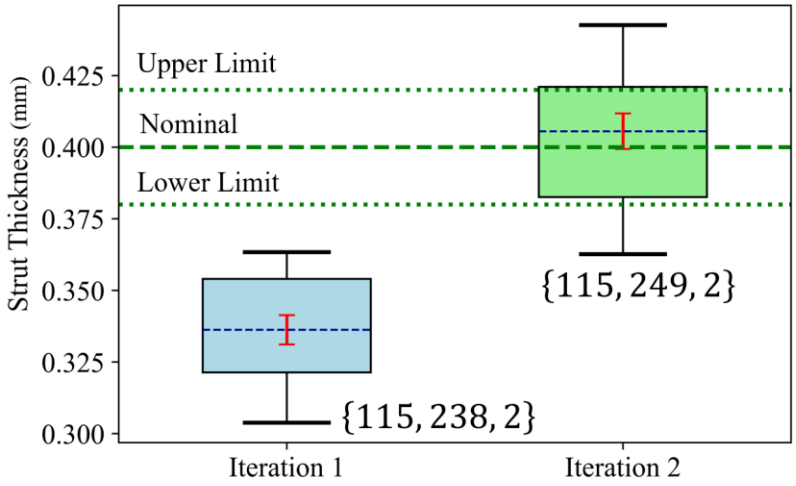

Figure 8: Box plotting of strut width with error bars for different iterations with optimized parameters $\{X_t^*, X_p^*, X_s^*\}$ to obtain nominal strut width.

5 Conclusions and Future Work

In this study, the parameter optimization of 3D-printed composite bone scaffolds using a new regression-minimization model offers a promising approach for achieving accurate and repeatable manufacturing. By leveraging data-driven techniques and optimization algorithms, this methodology enables the identification and fine-tuning of process parameters critical to scaffold fabrication. Through the utilization of DOE, image analysis for strut width characterization, and a modeling and optimization framework, the study successfully demonstrated the efficacy of the proposed approach. The regression-minimization model allowed for the efficient exploration of the parameter space, enabling the identification of optimal parameter combinations that resulted in the desired scaffold properties. By iteratively adjusting the parameters based on the feedback obtained from image analysis, the model guided the manufacturing process towards achieving the desired nominal strut width. The incorporation of a tolerance range around the target strut width further ensured that the final scaffolds met the required specifications.

This approach has significant implications for the field of bone tissue engineering as it enables the production of 3D printed composite bone scaffolds with improved accuracy and repeatability. The ability to precisely control the scaffold geometry and mechanical properties is crucial for successful bone regeneration applications. By optimizing the process parameters, it becomes possible to tailor the scaffold characteristics to meet specific patient needs and promote optimal tissue regeneration. Overall, the integration of data-driven methods, regression-minimization modeling, and parameter optimization techniques represents a significant step forward in the development of robust and reliable manufacturing processes for composite bone scaffolds. Continued research and advancements in this area hold great promise for further improving the quality, functionality, and clinical outcomes of 3D printed bone scaffolds, ultimately benefiting patients in need of bone tissue regeneration.

There are several future research directions: (i) developing more sophisticated models that take into account a wider range of variables and factors, such as the specific characteristics of the bone scaffold material and the printing process; (ii) validating the accuracy of the model by printing scaffolds and evaluating their mechanical properties, biocompatibility, and ability to support cell growth; (iii) expanding the optimization framework to consider multiple objectives simultaneously; and (iv) developing *in-situ* monitoring and control strategies to ensure the consistency and quality of the 3D printing process. Moreover, the strut segments supported by the previous layer are wider, and those are not considered in this study. The basic reason is that the overhanging strut widths are more important for maintaining the porosity structure of the overall scaffold. However, it is definitely beneficial to have a more comprehensive characterization of the entire struts over their whole length.

Acknowledgment

This work was partially sponsored by the National Science Foundation (No. CMMI-2046515).

References:

1. Zhang B, Wang L, Song P, Pei X, Sun H, Wu L, et al. 3D printed bone tissue regenerative PLA/HA scaffolds with comprehensive performance optimizations. Mater Des [Internet]. 2021;201:109490. Available from: https://doi.org/10.1016/j.matdes.2021.109490
2. Office of the Surgeon General. The Frequency of Bone Disease. In: Bone Health and Osteoporosis: A Report of the Surgeon General. 2004.
3. Wang W, Zhang B, Li M, Li J, Zhang C, Han Y, et al. 3D printing of PLA/n-HA composite scaffolds with customized mechanical properties and biological functions for bone tissue engineering. Compos Part B Eng. 2021;
4. Huiskes R, Weinans H, Van Rietbergen B. The relationship between stress shielding and bone resorption around total hip stems and the effects of flexible materials. Clin Orthop Relat Res. 1992;274:124–34.
5. Bai, Long, Gong, Cheng, Chen, Xiaohong, Sun, Yuanxi, Zhang, Junfang, Cai, Lecai, Zhu, Shengyan, Xie SQ. Additive Manufacturing of Customized Metallic. Metals (Basel). 2019;9:1004.
6. Roque R, Barbosa GF, Guastaldi AC. Design and 3D bioprinting of interconnected porous scaffolds for bone regeneration. An additive manufacturing approach. J Manuf Process. 2021;
7. Chia HN, Wu BM. Recent advances in 3D printing of biomaterials. J Biol Eng. 2015;9(1):1–14.
8. Eldokmak MM, Essawy MM, Abdelkader S. BIOLOGICAL AND MECHANICAL EVALUATION OF INTEGRATED NANO-HYDROXYAPATITE IN 3D-PRINTED POLYLACTIC ACID SCAFFOLD. Alexandria Dent J. 2024;(4):1–6.
9. Oladapo BI, Ismail SO, Zahedi M, Khan A, Usman H. 3D printing and morphological characterisation of polymeric composite scaffolds. Eng Struct. 2020;
10. Bahraminasab M. Challenges on optimization of 3D-printed bone scaffolds. Biomed Eng Online [Internet]. 2020;19(1):1–33. Available from: https://doi.org/10.1186/s12938-020-00810-2
11. Asadi-Eydivand M, Solati-Hashjin M, Farzad A, Abu Osman NA. Effect of technical parameters on porous structure and strength of 3D printed calcium sulfate prototypes. Robot Comput Integr Manuf. 2016;
12. Mazzoli A, Ferretti C, Gigante A, Salvolini E, Mattioli-Belmonte M. Selective laser sintering manufacturing of polycaprolactone bone scaffolds for applications in bone tissue engineering. Rapid Prototyp J. 2015;
13. Dimitrov D, Schreve K, De Beer N. Advances in three dimensional printing - State of the art and future perspectives. Rapid Prototyp J. 2006;
14. Hsu TJ, Lai WH. Manufacturing parts optimization in the three-dimensional printing process by the Taguchi method. J Chinese Inst Eng Trans Chinese Inst Eng A/Chung-kuo K Ch'eng Hsuch K'an. 2010;
15. Onuh SO, Hon KKB. Optimising build parameters for improved surface finish in stereolithography. Int J Mach Tools Manuf. 1998;

16. Srivastava M, Rathee S. Optimisation of FDM process parameters by Taguchi method for imparting customised properties to components. Virtual Phys Prototyp. 2018;
17. Lakshmi KS, Arumaikkannu G. Influence of process parameters on surface finish in customized bone implant using selective laser sintering. In: Advanced Materials Research. 2014.
18. Dorozhkin S V. Bioceramics of calcium orthophosphates. Biomaterials [Internet]. 2010;31(7):1465–85. Available from: http://dx.doi.org/10.1016/j.biomaterials.2009.11.050
19. Babilotte J, Martin B, Guduric V, Bareille R, Agniel R, Roques S, et al. Development and characterization of a PLGA-HA composite material to fabricate 3D-printed scaffolds for bone tissue engineering. Mater Sci Eng C [Internet]. 2021;118(August 2020):111334. Available from: https://doi.org/10.1016/j.msec.2020.111334
20. Bozkurt Y, Karayel E. 3D printing technology; methods, biomedical applications, future opportunities and trends. J Mater Res Technol [Internet]. 2021;14:1430–50. Available from: https://doi.org/10.1016/j.jmrt.2021.07.050
21. Wang X, Jiang M, Zhou Z, Gou J, Hui D. 3D printing of polymer matrix composites: A review and prospective. Composites Part B: Engineering. 2017.
22. Babilotte J, Guduric V, Le Nihouannen D, Naveau A, Fricain JC, Catros S. 3D printed polymer–mineral composite biomaterials for bone tissue engineering: Fabrication and characterization. Journal of Biomedical Materials Research - Part B Applied Biomaterials. 2019.
23. Tümer EH, Erbil HY. Extrusion-based 3d printing applications of pla composites: A review. Coatings. 2021.
24. Romani A, Suriano R, Levi M. Biomass waste materials through extrusion-based additive manufacturing: A systematic literature review. J Clean Prod. 2023;
25. Alonso-Fernández I, Haugen HJ, López-Peña M, González-Cantalapiedra A, Muñoz F. Use of 3D-printed polylactic acid/bioceramic composite scaffolds for bone tissue engineering in preclinical in vivo studies: A systematic review. Acta Biomaterialia. 2023.
26. Dong J, Lin P, Putra NE, Tümer N, Leeflang MA, Huan Z, et al. Extrusion-based additive manufacturing of Mg-Zn/bioceramic composite scaffolds. Acta Biomater. 2022;
27. Bai L, Gong C, Chen X, Sun Y, Zhang J, Cai L, et al. Additive manufacturing of customized metallic orthopedic implants: Materials, structures, and surface modifications. Metals. 2019.
28. Chen W, Nichols L, Brinkley F, Bohna K, Tian W, Priddy MW, et al. Alkali treatment facilitates functional nano-hydroxyapatite coating of 3D printed polylactic acid scaffolds. Mater Sci Eng C [Internet]. 2021;120(August 2020):111686. Available from: https://doi.org/10.1016/j.msec.2020.111686
29. Kazemi M, Mirzadeh M, Esmaeili H, Kazemi E, Rafienia M, Poursamar SA. Evaluation of the Morphological Effects of Hydroxyapatite Nanoparticles on the Rheological Properties and Printability of Hydroxyapatite/Polycaprolactone Nanocomposite Inks and Final Scaffold Features. 3D Print Addit Manuf. 2024;
30. Kim MH, Yun C, Chalisserry EP, Lee YW, Kang HW, Park SH, et al. Quantitative analysis of the role of nanohydroxyapatite (nHA) on 3D-printed PCL/nHA composite scaffolds. Mater Lett. 2018;
31. Ginestra PS, Rovetta R, Fiorentino A, Ceretti E. Bioprinting process optimization: Evaluation of parameters influence on the extrusion of inorganic polymers. In: Procedia

CIRP. 2020.

32. Khan Z, Kahin K, Rauf S, Ramirez-Calderon G, Papagiannis N, Abdulmajid M, et al. Optimization of a 3D bioprinting process using ultrashort peptide bioinks. Int J Bioprinting. 2019;
33. Tian S, Zhao H, Lewinski N. Key parameters and applications of extrusion-based bioprinting. Bioprinting. 2021.
34. Gao T, Gillispie GJ, Copus JS, Kumar APR, Seol YJ, Atala A, et al. Optimization of gelatin-alginate composite bioink printability using rheological parameters: A systematic approach. Biofabrication. 2018;
35. Webb B, Doyle BJ. Parameter optimization for 3D bioprinting of hydrogels. Bioprinting. 2017;
36. Butler HM, Naseri E, MacDonald DS, Andrew Tasker R, Ahmadi A. Optimization of starch- and chitosan-based bio-inks for 3D bioprinting of scaffolds for neural cell growth. Materialia. 2020;
37. Gong Y, Wang F, Al-Furjan MSH, Shan L, He J, Bian X, et al. Experimental investigation and optimal 3D bioprinting parameters of sa-gel porous cartilage scaffold. Appl Sci. 2020;
38. Law ACC, Wang R, Chung J, Kucukdeger E, Liu Y, Barron T, et al. Process parameter optimization for reproducible fabrication of layer porosity quality of 3D-printed tissue scaffold. J Intell Manuf. 2023;
39. De Stefano P, Briatico-Vangosa F, Bianchi E, Pellegata AF, De Hartungen AH, Corti P, et al. Bioprinting of matrigel scaffolds for cancer research. Polymers (Basel). 2021;
40. James S, Mulgaonkar S. Study on parameter optimization of 3D bioprinting of hybrid bio-inks. Int J Adv Manuf Technol. 2022;
41. Rashia Begum S, Saravana Kumar M, Pruncu CI, Vasumathi M, Harikrishnan P. Optimization and Fabrication of Customized Scaffold Using Additive Manufacturing to Match the Property of Human Bone. J Mater Eng Perform. 2021;
42. Sun J, Yao K, Huang K, Huang D. Machine learning applications in scaffold based bioprinting. Mater Today Proc. 2022;
43. Bagheri Saed A, Behravesh AH, Hasannia S, Alavinasab Ardebili SA, Akhoundi B, Pourghayoumi M. Functionalized poly L-lactic acid synthesis and optimization of process parameters for 3D printing of porous scaffolds via digital light processing (DLP) method. J Manuf Process. 2020;
44. Pulipaka A, Gide KM, Beheshti A, Bagheri ZS. Effect of 3D printing process parameters on surface and mechanical properties of FFF-printed PEEK. J Manuf Process. 2023;
45. Tian Y, Ren H, He J, Zha X, Lin K, Zhou M, et al. Surface roughness improvement of Ti-6Al-4V alloy overhang structures via process optimization for laser-powder bed fusion. J Manuf Process. 2024;
46. Singh J, Singh G, Pandey PM. Multi-objective optimization of solvent cast 3D printing process parameters for fabrication of biodegradable composite stents. Int J Adv Manuf Technol. 2021;115(11–12):3945–64.
47. Khalili S, Khorasani SN, Saadatkish N, Khoshakhlagh K. Characterization of gelatin/cellulose acetate nanofibrous scaffolds: Prediction and optimization by response surface methodology and artificial neural networks. Polym Sci - Ser A. 2016;
48. Das R, Bhasarkar J, Rastogi A, Saxena R, Bal DK. Artificial neural network-based pore size prediction of alginate gel scaffold for targeted drug delivery. Neural Comput Appl. 2023;

49. Mondal B, Mandal N, Mondal S, Mukherjee K, Mukhopadhyay S, Dey A. Optimisation of process parameters for fabrication of nanocrystalline TiO2-hydoxyapatite based scaffold using response surface methodology. Adv Appl Ceram. 2014;
50. Adeli H, Sharif Zein SH, Tan SH, Ahmad AL. Optimization of the mechanical strength properties of poly(L-lactide)/ multi-walled carbon nanotube scaffolds using response surface methodology. Nano. 2011;
51. Park HS, Nguyen DS, Le-Hong T, Van Tran X. Machine learning-based optimization of process parameters in selective laser melting for biomedical applications. J Intell Manuf. 2022;
52. Rahmani Dabbagh S, Ozcan O, Tasoglu S. Machine learning-enabled optimization of extrusion-based 3D printing. Methods. 2022;
53. Liu C, Wang L, Lu W, Liu J, Yang C, Fan C, et al. Computer vision-aided bioprinting for bone research. Bone Res. 2022;10(1):1–14.
54. Conev A, Litsa E, Perez M, Diba M, Mikos AG, Kavraki L. Machine Learning Guided 3D Printing of Tissue Engineering Scaffolds. Tissue Eng Part A. 2020;
55. Wang Y, Huang J, Wang Y, Feng S, Peng T, Yang H, et al. A CNN-based Adaptive Surface Monitoring System for Fused Deposition Modeling. IEEE/ASME Trans Mechatronics. 2020;25(5):1–1.
56. Yu C, Jiang J. A perspective on using machine learning in 3D bioprinting. Int J Bioprinting. 2020;6(1):4–11.
57. Cohen DL, Lipton JI, Bonassar LJ, Lipson H. Additive manufacturing for in situ repair of osteochondral defects. Biofabrication. 2010;2(3).
58. Zhu Z, Guo SZ, Hirdler T, Eide C, Fan X, Tolar J, et al. 3D Printed Functional and Biological Materials on Moving Freeform Surfaces. Adv Mater. 2018;30(23):1–8.
59. Collier E, Maitland B, Sanderson RW, Shiroud Heidari B, Lamb C, Hepburn MS, et al. In Situ Characterization of Melt–Electrowritten Scaffolds in 3D Using Optical Coherence Tomography. Adv Photonics Res. 2022;2100274:2100274.
60. Jin Z, Zhang Z, Gu GX. Autonomous in-situ correction of fused deposition modeling printers using computer vision and deep learning. Manuf Lett [Internet]. 2019;22:11–5. Available from: https://doi.org/10.1016/j.mfglet.2019.09.005
61. Bozkir A, Saka OM. Formulation and investigation of 5-FU nanoparticles with factorial design-based studies. Farmaco. 2005;
62. Kumar L, Sreenivasa Reddy M, Managuli RS, Pai K. G. Full factorial design for optimization, development and validation of HPLC method to determine valsartan in nanoparticles. Saudi Pharm J [Internet]. 2015;23(5):549–55. Available from: http://dx.doi.org/10.1016/j.jsps.2015.02.001
63. Liu S, Zhang C, Hong P, Ji H. Concentration of docosahexaenoic acid (DHA) and eicosapentaenoic acid (EPA) of tuna oil by urea complexation: Optimization of process parameters. J Food Eng. 2006;73(3):203–9.
64. Aslan V, Eryilmaz T. Polynomial regression method for optimization of biodiesel production from black mustard (Brassica nigra L.) seed oil using methanol, ethanol, NaOH, and KOH. Energy [Internet]. 2020;209:118386. Available from: https://doi.org/10.1016/j.energy.2020.118386
65. Zhu C, Byrd RH, Lu P, Nocedal J. Algorithm 778: L-BFGS-B: Fortran Subroutines for Large-Scale Bound-Constrained Optimization. ACM Trans Math Softw. 1997;23(4):550–60.

66. Gelman A, Carlin JB, Stern HS, Dunson DB, Vehtari A, Rubin DB. Bayesian data analysis. Chapman and Hall/CRC. Bayesian Data Analysis, Third Edition. 2013.
67. Friedman J, Hastie T, Tibshirani R. The elements of statistical learning. New York, NY, USA: Springer New York Inc. Springer series in statistics New York. 2001.
68. Barbur VA, Montgomery DC, Peck EA. Introduction to Linear Regression Analysis. Stat. 1994;
69. Iguyon I, Elisseeff A. An introduction to variable and feature selection. Journal of Machine Learning Research. 2003.
70. Peng X, Huo Y, Zhang G, Cheng L, Lu Y, Li J, et al. Controlled mechanical and mass-transport properties of porous scaffolds through hollow strut. Int J Mech Sci. 2023;
71. Boeder NF, Dörr O, Bauer T, Mattesini A, Elsässer A, Liebetrau C, et al. Impact of strut thickness on acute mechanical performance: A comparison study using optical coherence tomography between DESolve 150 and DESolve 100. Int J Cardiol. 2017;
72. Seehanam S, Khrueaduangkham S, Sinthuvanich C, Sae-Ueng U, Srimaneepong V, Promoppatum P. Evaluating the effect of pore size for 3d-printed bone scaffolds. Heliyon [Internet]. 2024;10(4):e26005. Available from: https://doi.org/10.1016/j.heliyon.2024.e26005
73. Dias MR, Guedes JM, Flanagan CL, Hollister SJ, Fernandes PR. Optimization of scaffold design for bone tissue engineering: A computational and experimental study. Med Eng Phys [Internet]. 2014;36(4):448–57. Available from: http://dx.doi.org/10.1016/j.medengphy.2014.02.010